JOURNAL OF GEOPHYSICAL RESEARCH, VOL. 104, NO. D20, PAGES 24,471–24,484, OCTOBER 27, 1999

# Global climatology of abundance and solar absorption of oxygen collision complexes

Charles S. Zender[1]

National Center for Atmospheric Research, Boulder, Colorado

**Abstract.** To improve our understanding of the absorption of solar radiation in the atmosphere we have characterized the spectral absorption, the spatial and temporal abundance, and the radiative forcing of the oxygen collision pairs $O_2{\cdot}O_2$ and $O_2{\cdot}N_2$ ($O_2{\cdot}X \equiv O_2{\cdot}O_2 + O_2{\cdot}N_2$). The regional, vertical, seasonal, and annual patterns of $O_2{\cdot}X$ abundance and radiative forcing are obtained from a general circulation model. We estimate the mean absorption by $O_2{\cdot}X$, heretofore neglected in large scale atmospheric models, is 0.75–1.2 W m$^{-2}$, or 1–2% of total atmospheric solar absorption. $O_2{\cdot}X$ absorption reduces surface insolation by 0.48–0.78 W m$^{-2}$ and increases the net radiative flux at the tropopause by 0.32–0.52 W m$^{-2}$. These ranges bracket the uncertainties due to spectral absorption cross sections, $O_2{\cdot}N_2$ efficiency, $O_2{\cdot}X$ abundance, and cloud distribution. Globally averaged, $O_2{\cdot}X$ enhances absorption equally in clear and in cloudy skies.

We create a global climatology of well-mixed collision complex abundances by scaling $O_2{\cdot}X$ abundance to other complexes such as $N_2{\cdot}N_2$ and $O_2{\cdot}Ar$. Collision complex abundance depends quadratically on the concentrations of the constituents. This dependence causes a 20% increase in $O_2{\cdot}X$ abundance in the Arctic relative to the Tropics for the same sea level pressure. The variations in zonal mean $O_2{\cdot}X$ abundance due to surface elevation, the annual mean meridional temperature gradient, and to seasonal temperature variations are 40, 15, and 10%, respectively. $O_2{\cdot}X$ heating obeys the weakly absorbing, linear limit so it peaks at the surface in clear skies, but clouds shift this peak up by 200–300 mb on seasonal timescales. Surface albedo and clouds strongly modulate the solar forcing efficiency of $O_2{\cdot}X$ (forcing per unit abundance) by altering the mean photon path length. These factors produce annual mean forcing maxima in the subtropics over bright deserts and regions of marine stratus. Inclusion of $O_2{\cdot}X$ in models is likely to reduce cold biases in the summertime polar atmosphere, where $O_2{\cdot}X$ contributes 2–4% of total solar heating.

## 1. Introduction

Our ability to balance the solar radiation budget of the atmosphere is uncertain [e.g., **????**, and references therein]. Until we can perform this fundamental task, our skill at predicting the all sky radiation budget, and hence at predicting climate and climate change, will continue to be highly uncertain [e.g., **?**]. The atmospheric collision complexes of oxygen $O_2{\cdot}O_2$ and $O_2{\cdot}N_2$ (henceforth $O_2{\cdot}X \equiv O_2{\cdot}O_2 + O_2{\cdot}N_2$) have recently been identified as contributors to discrepancies between modeled and observed surface insolation [**??**]. $O_2{\cdot}X$ presents a timely and interesting case for a radiative budget study because its solar absorption cross sec-

[1]Now at Department of Earth System Science, University of California at Irvine.



Paper number 1999JD900797.
0148-0227/99/1999JD900797$09.00

tion is relatively well known, but its abundance and absorption have not been characterized at the global scale necessary to fully describe its impact on climate.

The absorption features of oxygen collision complexes have been studied in the laboratory and in the atmosphere for many decades [**??**, and references therein]. Collisions relax the selection rules for dipole-forbidden transitions in one or both $O_2$ molecules, allowing for absorption during the collision. The detection of discrepancies between modeled and observed solar radiation in cloudy skies [**??**] provoked interest in whether $O_2{\cdot}X$ contributes to this discrepancy [**??**] and in what its global radiative forcing characteristics are.

**?** first estimated the global annual mean solar absorption by $O_2{\cdot}O_2$ in clear sky and in all sky (i.e., including clouds) conditions as 0.53 and 0.57 W m$^{-2}$, respectively. Two newer estimates include the effects of the powerful 1.27 μm band and of nitrogen induced absorption ($O_2{\cdot}N_2$) in this band. Estimates from these studies suggest that globally and annually averaged, $O_2{\cdot}X$ absorbs 0.9–1.3 W m$^{-2}$ [**?**] or 0.84 W m$^{-2}$ [**?**]. Thus $O_2{\cdot}X$ is thought to contribute 1–2% of the total solar atmospheric absorption of 67 W m$^{-2}$ (out of 342 W m$^{-2}$ incoming) [**?**]. These estimates of $O_2{\cdot}X$ absorption are based on single column line-by-line, multiple-scattering radiative transfer models which have been extensively validated against atmospheric observations by high spectral resolution instruments. The disparity in the latter two estimates is mostly due to uncertainties in absorption cross sections for $O_2{\cdot}X$ bands in the near infrared and, to a lesser extent, from extrapolating single-column results to global annual means.

We use the term "radiative forcing" to denote various measures of the influence of atmospheric heating by $O_2{\cdot}X$ on the climate system. Line-by-line estimates of $O_2{\cdot}X$ absorption are too computationally expensive to convey the rich regional and seasonal behavior of $O_2{\cdot}X$ radiative forcing caused by variations in temperature, pressure, elevation, clouds, surface albedo, and mixing ratios of other radiatively active atmospheric constituents. A general circulation model (GCM) is best suited to provide self-consistent, time-varying realistic distributions of $O_2{\cdot}X$ forcing. Employing a GCM allows us to extend prior studies and to provide additional forcing metrics, including clear versus cloudy sky forcing, surface forcing, and net forcing at the tropopause. These metrics allow us to compare the radiative forcing by $O_2{\cdot}X$ to other absorbers, including greenhouse gases. These comparisons, in turn, help to prioritize implementation of $O_2{\cdot}X$ physics in large-scale atmospheric models. It is worthwhile noting that in contrast to anthropogenically influenced greenhouse gas concentrations, $O_2{\cdot}X$ abundance is not changing.

To our knowledge no prior study has constructed a systematic global climatology for any collision complex (or dimer). Moreover, the regional, seasonal, and vertical patterns of $O_2{\cdot}X$ abundance generalize to all complexes formed from well-mixed gases. Thus these patterns, which depend mainly on the meridional temperature gradient and orographic features, apply to all well-mixed collision complexes, for example, $N_2{\cdot}N_2$, $O_2{\cdot}Ar$, and $O_2{\cdot}CO_2$. The patterns of $O_2{\cdot}X$ radiative forcing, which depend additionally on insolation, surface albedo, and cloud cover, only apply to other complexes with absorption features similar to those of $O_2{\cdot}X$. Thus, by characterizing $O_2{\cdot}X$ abundance and forcing, we automatically obtain insight into all well-mixed collision complexes.

Establishing the spatial and temporal patterns of $O_2{\cdot}X$ abundance and forcing will also help future studies ascertain whether unexplained atmospheric solar absorption is consistent with absorption by collision complexes (or dimers) of well-mixed molecules. The existence of complexes besides $O_2{\cdot}X$ which cause significant solar radiative forcing is highly speculative. All significant structured atmospheric absorption measured in the atmosphere for large portions of the solar spectrum has been convincingly attributed to known absorbers [**????**]. Moreover, a number of recent field studies explains all observed broadband clear sky solar absorption to within the uncertainties in the observations and models [**????**]. However, **?** and **?** find inexplicable discrepancies between models and observations of the clear sky diffuse field, and many independent studies show enhanced cloudy sky solar absorption relative to model predictions on both local and global scales [**???**]. Since $O_2{\cdot}X$ has been proposed as a candidate for explaining some of these discrepancies [**??**], this study attempts to bound the role of $O_2{\cdot}X$ in explaining enhanced absorption in clear and cloudy skies.

The remainder of this study is organized as follows: Section 2 presents the nomenclature of collision complexes and summarizes the laboratory measurements of $O_2{\cdot}X$ cross sections. Section 3 illustrates the modeled spectral characteristics of $O_2{\cdot}X$ absorption during a field campaign and shows its net vertical heating signature in an idealized atmosphere. Section 4 presents the regional, seasonal, and vertical climatologies of $O_2{\cdot}X$ abundance and forcing and generalizes $O_2{\cdot}X$ abundance to other well-mixed collision complexes. Section 5 summarizes the results and discusses their implication for future studies of the atmosphere.

## 2. Characterization of Abundance and Absorption Cross Section

Quantifying the global radiative forcing of a gaseous molecular species $i$ requires characterization of both its concentration $n_i(x, y, z, t)$ molecule cm$^{-3}$ and its absorption cross

section $\sigma_i(\lambda)\,\mathrm{cm}^2$ molecule$^{-1}$. The convolution of these two quantities with the instantaneous radiation field yields the instantaneous forcing due to the gas. However, careful laboratory measurements provide convincing evidence that for atmospheric temperatures and solar wavelengths, $O_2$·X absorption is due to transient collision complexes rather than bound dimers (or van der Waals complexes) [**??**]. Since $O_2$·X is not a bound molecule, we begin by defining properties analogous to $n_i$ and $\sigma_i$, but that apply to collision complexes.

### 2.1. Abundance

The "abundance" $n_{X\cdot Y}$ of a collision complex of molecules X and Y is analogous to a traditional number concentration of a molecular species. We define $n_{O_2\cdot X} \equiv n_{O_2} n_X$ where $n_{O_2}$ and $n_X$ are the number concentrations of $O_2$ and of its collision partner ($N_2$ or $O_2$, unless otherwise specified) in molecule cm$^{-3}$, respectively. Thus the dimensions of $n_{O_2\cdot X}$ are molecule$^2$ cm$^{-6}$. By definition, $n_{O_2\cdot X}$ is linearly proportional to the frequency of collisions of $O_2$ with X. To graphically depict the total column abundance of $O_2$·X, we will present the vertical column paths $N_{O_2\cdot X}$ defined by

$$\begin{aligned} N_{O_2\cdot O_2} &\equiv \int_0^{\mathrm{TOA}} n_{O_2\cdot O_2}\,dz = \int_0^{\mathrm{TOA}} n_{O_2}^2\,dz \\ N_{O_2\cdot N_2} &\equiv \int_0^{\mathrm{TOA}} n_{O_2} n_{N_2}\,dz = \gamma N_{O_2\cdot O_2} \end{aligned} \tag{1}$$

where the integration over $z$ (height) is from the surface ($z = 0$) to the top of atmosphere (TOA $\approx 1.5$ mb due to GCM vertical discretization). Likewise, the column path of a molecule X, in molecule cm$^{-2}$, will be denoted by $N_X$. We assume in (1) that the volume mixing ratios of $N_2$ and $O_2$ are constant in the Earth's atmosphere and that their ratio is the constant $\gamma \equiv n_{N_2}/n_{O_2} = 3.72787$ [**?**, p. 9]. Since the vertical profile of $n_{O_2\cdot X}$ varies with the square of atmospheric density, variations in $\gamma$ above the stratosphere have negligible impact on the column abundance, and thus forcing, of $O_2$·X.

### 2.2. Absorption Cross Sections

The absorption bands of the $O_2$·$O_2$ and $O_2$·$N_2$ collision complexes have been studied for decades. **?** give an excellent review of laboratory research on oxygen collision complex absorption. Here we summarize only the research necessary to understand the physical parameterizations and uncertainties present in this study.

Laboratory measurements of $O_2$·X absorption infer a binary absorption coefficient $\sigma^b(\lambda)$ from the quadratic dependence of measured absorption on $O_2$ concentration, $n_{O_2}$. **?** provide a detailed description of this type of measurement and its uncertainties. The dimensions of $\sigma^b(\lambda)$ are cm$^5$ molecule$^{-2}$. Thus, for a given concentration $n_{O_2}$ molecule cm$^{-3}$ and path length $\Delta z$ centimeters of collision partner ($O_2$ or $N_2$), the optical depths $\tau_{O_2\cdot X}$ due to $O_2$·X at wavelength $\lambda$ are

$$\begin{aligned} \tau_{O_2\cdot O_2}(\lambda) &= \sigma^b_{O_2\cdot O_2}(\lambda)\, n_{O_2}^2 \Delta z \qquad (2) \\ \tau_{O_2\cdot N_2}(\lambda) &= \sigma^b_{O_2\cdot N_2}(\lambda)\, n_{O_2} n_{N_2} \Delta z \\ &= \gamma\, \epsilon_{N_2} \sigma^b_{O_2\cdot O_2}(\lambda)\, n_{O_2}^2 \Delta z \\ \tau_{O_2\cdot N_2}(\lambda) &= \gamma\, \epsilon_{N_2} \tau_{O_2\cdot O_2}(\lambda) \qquad (3) \end{aligned}$$

where (3) applies to the 1.27 µm band only (see Plate 1) and $\epsilon_{N_2}$, discussed below, is the efficiency of $N_2$ (relative to $O_2$) at inducing $O_2$ absorption through collisional processes (i.e., $\sigma^b_{O_2\cdot N_2} = \epsilon_{N_2} \sigma^b_{O_2\cdot O_2}$).

Plate 1 shows the solar absorption continua for $O_2$·X measured by **?** at $\sim 0.15$ nm resolution for $0.335 < \lambda < 1.137$ µm. The 1.27 µm band has not been adequately examined with modern laboratory techniques, so we adopt the cross sections for this band recommended by **?**. On the basis of a number of earlier measurements, Solomon et al. constructed the 1.27 µm band by stretching the measured 1.06 µm band to a full width at half maximum (FWHM) of 180 cm$^{-1}$ and scaling its integrated band intensity by 1.6. The cross sections of $O_3$ and $O_2$ [**?**], and of $NO_2$ [**?**], are shown for comparison. The red curves show that significant $O_2$·$O_2$ solar absorption occurs in two spectral regions: $0.3 < \lambda < 0.7$ µm and $1.0 < \lambda < 1.4$ µm. $O_2$·$O_2$ visible absorption is due to simultaneous collision induced transitions in both $O_2$ molecules, while near-infrared absorption involves only one $O_2$ transition.

**?** recently measured $\sigma^b_{O_2\cdot O_2}$ for $0.455 < \lambda < 0.830$ µm and compared their measurements to those of **?** (Plate 1). The maximum $\sigma^b_{O_2\cdot O_2}$ and the integrated band intensities of most bands differed by $< 20\%$ between the two sets of measurements. Greenblatt et al. found the integrated band intensity of the bands centered at 360, 380, and 477 nm varied by $< 15\%$ from $T = 296$ K to 196 K. Newnham and Ballard found the integrated band intensity of four bands from 532–630 nm varied by $< 10\%$ from $T = 283$ K to 223 K but that the intensity of the 477 nm band decreased by 30% over this temperature range. Thus the two studies disagree on the temperature dependence of the the only band examined in both studies, the 477 nm band. Why the disagreement at 477 nm exceeds the stated error bars of the two studies is unexplained. Balloon-borne observations of the 447, 532, and 577 nm bands by **?** recorded a 20% decrease in $\sigma^b_{O_2\cdot O_2}$ as the temperature increased from $T = 200$ K to 300 K. Note that this decrease is in contrast to the increase of $\sigma^b_{O_2\cdot O_2}$ with $T$ measured by Newnham and Ballard in the 477 nm band.

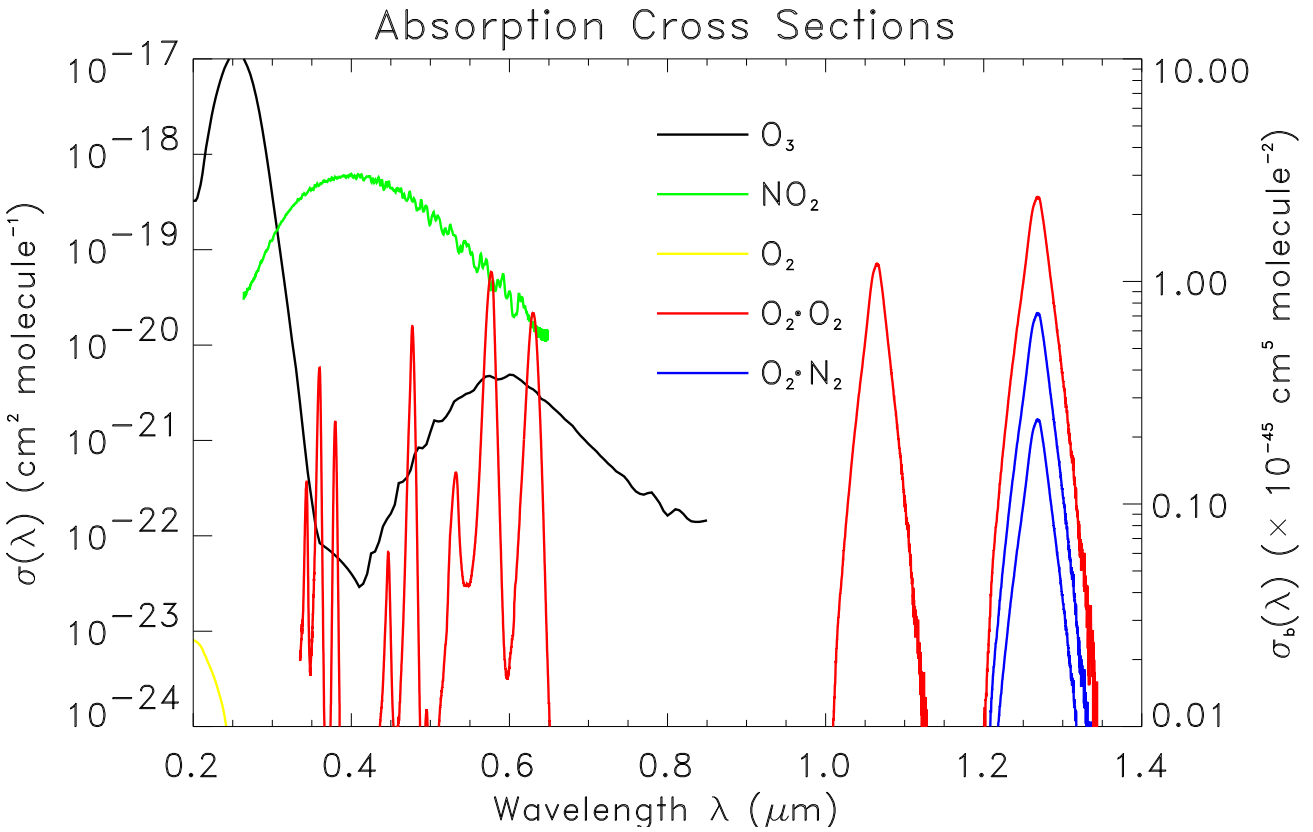


**Plate 1.** Solar absorption continua of $O_2{\cdot}X$, $O_3$, $O_2$, and $NO_2$. Continua of $O_2{\cdot}O_2$ (red) and $O_2{\cdot}N_2$ (blue) are plotted as binary absorption coefficients $\sigma^b_{O_2\cdot X}$ (cm$^5$ molecule$^{-2}$) on the right-hand axis. Continua of $O_3$ (black), $NO_2$ (green), and $O_2$ (yellow) are plotted as traditional cross sections $\sigma$ (cm$^2$ molecule$^{-1}$) on the left-hand axis.

Osterkamp et al. conclude that $O_2{\cdot}O_2$ may be a metastable complex with some dimer-like properties. For simplicity, our study assumes $\sigma^b_{O_2\cdot X}$ is constant with temperature. However, we should remain open to the possibility that $\sigma^b_{O_2\cdot X}$ varies significantly with temperature for some bands.

The parameter $\epsilon_{N_2}$ defines the efficiency of $N_2$ relative to $O_2$ as a partner for inducing absorption in the $O_2$ 1.27 µm band. The upper and lower blue curves centered at $\lambda = 1.27$ µm in Plate 1 correspond to $\sigma^b_{O_2\cdot N_2}$ assuming $\epsilon_{N_2} = 0.1$ and 0.3, respectively. All prior studies show $0.1 \leq \epsilon_{N_2} \leq 0.3$, and the preponderance suggest $\epsilon_{N_2} = 0.3$ (see discussion by **?**).

**?** used differential optical absorption spectroscopy at large zenith angles to show their high spectral resolution ($\approx$ 0.6 nm) in situ measurements agree with the laboratory cross sections of **?** (Plate 1) to within 0.3% for the $O_2{\cdot}O_2$ band at 0.63 µm. **?** recently inferred $\sigma^b_{O_2\cdot X}$ for $1.0 < \lambda < 1.57$ µm from field measurements with a high-resolution (0.6 cm$^{-1}$) interferometer. They inferred comparable peak intensities in the 1.06 and 1.27 µm $O_2{\cdot}X$ bands, but narrower FWHMs, than previous investigators [**?**]. These narrower FWHMs would reduce absorption in the near-infrared $O_2{\cdot}X$ bands by about 30% relative to Greenblatt et al. and Solomon et al.

The uncertainties in $\sigma^b_{O_2\cdot X}(\lambda)$ contribute roughly half of the uncertainty in our estimate of global $O_2{\cdot}X$ forcing. The uncertainty in $\sigma^b_{O_2\cdot X}(\lambda)$ is $< 10\%$ for $0.335 < \lambda < 1.137$ µm [**?**]. Uncertainty in 1.27 µm band absorption is $\sim 30\%$. This was estimated by extrapolating to global scale the difference between single-column simulations employing the continua proposed by **?** and by **?**. For consistency, our study adopts the same cross sections as Solomon et al., but we note two choices that keep our results for total $O_2{\cdot}X$ absorption closer to those of Mlawer et al. First, we use $\epsilon_{N_2} = 0.2$, a somewhat conservative value. Second, we neglect the $O_2{\cdot}O_2$ absorption band near 1.58 µm. This band absorbs $\sim 9\%$ as much as the 1.27 µm band [**?**]. Appending

the 1.58 µm continuum to the Solomon et al. cross sections would increase our computed total $O_2$·X solar forcing by $\sim 4\%$. Other absorption features of $O_2$·X are negligible in terms of the total absorbed solar irradiance. These features, and those of many other well-mixed collision complexes, are summarized in Table 1.

## 3. High Resolution Single Column Simulations

$O_2$·X complexes are a relatively recent addition to the longstanding group of solar absorbers considered in large-scale atmospheric models: $H_2O$, $O_3$, $O_2$, $NO_2$, and $CO_2$. As such, the spectrally and vertically dependent features of $O_2$·X absorption have not yet been thoroughly characterized in the literature. We now analyze these features in high-resolution, single-column simulations in order to better understand their implications on global-annual scales.

### 3.1. Spectral Characteristics and Overlap

Two previous studies characterized aspects of the spectral overlaps between $O_2$·X and more familiar absorbers. **?** [**?**, Figure 2] show $O_2$·X spectral features at surface and TOA for $335 < \lambda < 1137$ nm. **?** [**?**, Figure 2] show residual surface absorption spectra of $O_2$·$O_2$, $O_2$, and $H_2O$ in the region $610 < \lambda < 680$ nm. To complement these studies, our Plate 2 shows the modeled absorption optical depth $\tau_{\rm abs}(\lambda)$ of all significant gaseous solar absorbers for $200 < \lambda < 1400$ nm. The spectra represent local solar noontime (solar zenith angle $\theta = 45.128°$) for October 15, 1995, at the Clouds and Radiation Testbed (CART) site in Oklahoma. This was a pristine day with minimal aerosol burden ($0.04 < \tau^{\rm aer}_{0.5\mu} < 0.05$, not shown), low precipitable water (11.6 kg m$^{-2}$), low column $O_3$ (233 DU), and estimated column $NO_2$ of $5 \times 10^{19}$ m$^{-2}$. **?** describe the multistream narrow band (10 cm$^{-1}$) Malkmus model, the experimental uncertainties, and all the input data in more detail.

Plate 2 isolates the solar absorption continuum (using $\sigma^b_{\rm O_2\cdot X}$ from Plate 1) of each gaseous absorber considered in the model. $O_2$·X shares with $H_2O$ the distinction of overlapping with all the significant solar absorbers. The strongest visible bands of $O_2$·$O_2$ overlap with the center of the $O_3$ Chappuis bands near 0.6 µm. The $O_2$·$O_2$ band at 0.630 µm overlaps the discrete $O_2$ $\gamma$ band at 0.629 µm. The strong 1.06 µm band partially overlaps a saturated water vapor band, but its center is the strongest nonoverlapped feature of $O_2$·$O_2$ in the spectrum. Absorption at 1.27 µm shows strong overlap among the oxygen infrared band, $O_2$·$O_2$, and $O_2$·$N_2$. Although 1.27 µm is in a water vapor window, both wings of the $O_2$·X bands centered there overlap with weak $CO_2$ bands and with the wings of $H_2O$ bands. This overlap with $H_2O$ lessens somewhat in dry air masses where column moisture is $< 5$ kg m$^{-2}$ (e.g., Antarctica), but $O_2$·X absorption is only weakly sensitive to variations in $H_2O$ (see section 4.3). As Plate 2 shows, contributions of $O_2$·$N_2$ and $O_2$·$O_2$ to the total 1.27 µm continuum are nearly equal if $\epsilon_{N_2} = 0.2$. Using $\epsilon_{N_2} = 0.3$ (and weaker $\sigma^b_{\rm O_2\cdot X}(1.27\,\mu{\rm m})$), **?** found $O_2$·$N_2$ absorption may exceed $O_2$·$O_2$ absorption in this band by 15%.

The $O_2$·$O_2$ band at 0.477 µm occupies a relatively transparent spectral region where it is often stronger than any other gaseous absorber, i.e., $O_3$ or $NO_2$. This band is discernible in routine optical depth spectra taken at the CART site and other locations [**?**]. Note that neglecting $O_2$·$O_2$ absorption in its stronger bands could bias operational retrievals of other absorber amounts (e.g., $O_3$, $NO_2$, or aerosol), leading to overestimates of order 0.01 optical depths. Fortunately, we are aware of no operational retrievals that are compromised by neglect of $O_2$·$O_2$ absorption. For this particular profile, we estimate $O_2$·X causes 2.3 W m$^{-2}$, or 1.4%, of the total modeled atmospheric solar absorption of 164 W m$^{-2}$. Accounting for this absorption reduces the discrepancy between noontime modeled and observed surface insolation (773 and 760 W m$^{-2}$, respectively) from 13.0 to 11.2 W m$^{-2}$ [**?**].

### 3.2. Vertical Heating Profile

To illustrate the vertical profile of $O_2$·X heating, we simulated "climatological" clear and cloudy sky, aerosol-free heating profiles for a 92 level midlatitude summer atmosphere [**?**]. Figure 1 shows the resulting vertical profile of total solar heating for the clear sky profile, the $O_2$·X contribution to this clear sky heating, and the $O_2$·X cloudy sky heating. The solar zenith angle ($\theta = 60°$), surface albedo ($A = 0.2$), and cloud properties (100 mbthick liquid stratus cloud centered at 850 mb, condensate path 100 g m$^{-2}$) represent climatological atmospheric properties. The $O_2$·X heating profiles are multiplied by a factor of 100 for clarity.

The clear sky $O_2$·X heating increases rapidly with pressure, peaking at the surface. Thus $O_2$·X clear sky heating weakly destabilizes the atmospheric column. At moderate zenith angles, $O_2$·X absorption is relatively weak (i.e., $\tau_{\rm O_2\cdot X} < 0.1$) and is not dominated by overlap with other gases (Plate 2). Heating by a well-mixed molecule in this nonoverlapped, optically thin limit is constant with air density. In constrast, it is easy to show that in this limit, heating by a well-mixed collision complex (or dimer) increases linearly with air density. The high correlations of the $O_2$·X heating in Figure 1 with air density (not shown) confirm that $O_2$·X heating obeys the weakly absorbing linear limit in both clear and cloudy skies. The absorbed energy actually increases quadratically with dry air density, i.e., linearly with $O_2$·X abundance (1), but one factor of density (the heat

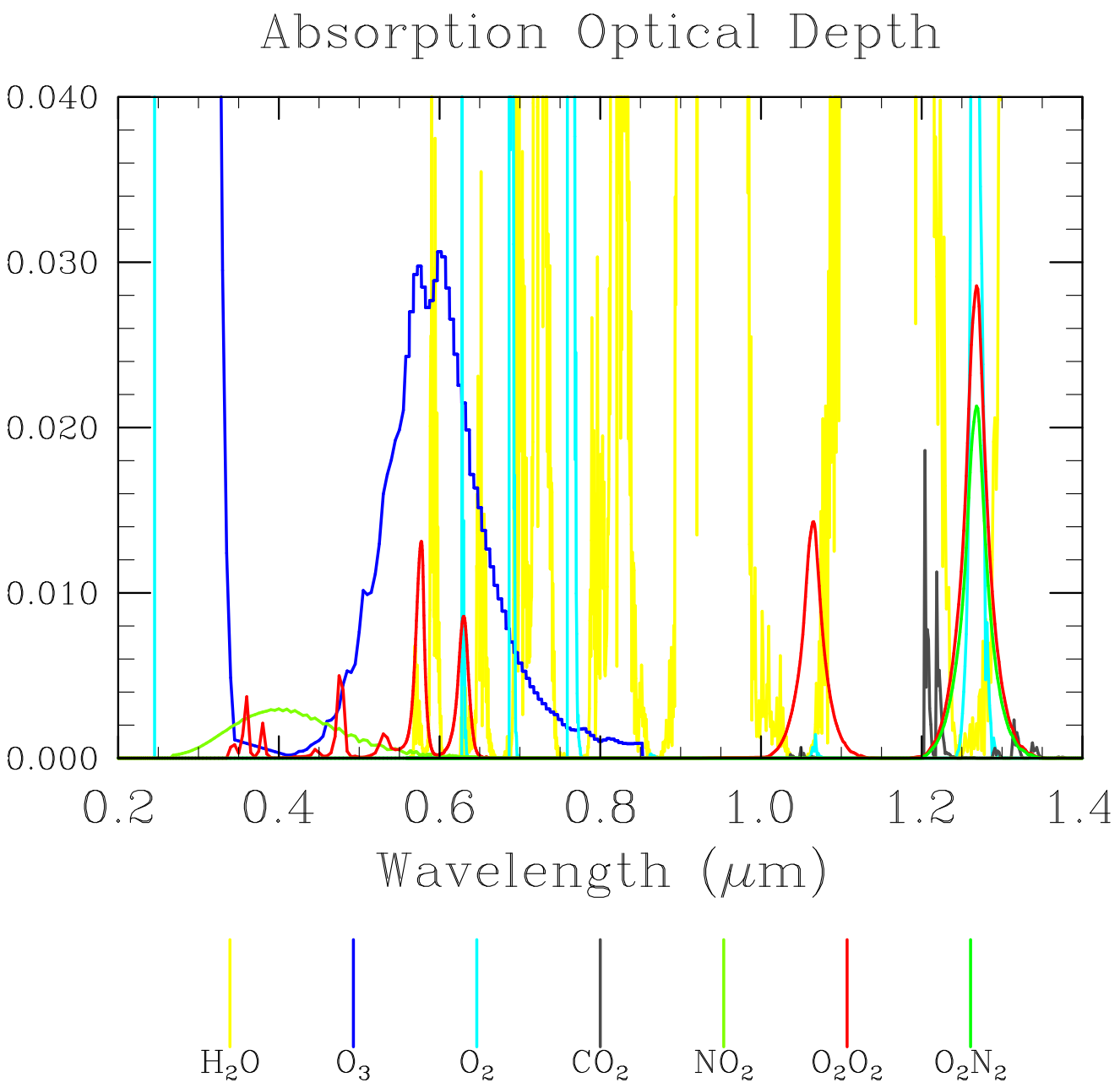


**Plate 2.** Decomposition of simulated absorption optical depth $\tau_{\rm abs}(\lambda)$ at the CART site at local solar noontime on October 15, 1995. Gaseous absorbers included are $O_2{\cdot}O_2$ (red), $O_2{\cdot}N_2$ (green), $H_2O$ (yellow), $O_3$ (blue), $O_2$ (light blue), $NO_2$ (light green), and $CO_2$ (black). The line spectra of $H_2O$, $CO_2$, and $O_2$ are averaged over 10 $cm^{-1}$.

capacity of air in J $m^{-3}$ $K^{-1}$) is removed in converting from a volumetric heating (W $m^{-3}$) to an absolute heating rate (K $d^{-1}$). We note that $O_2{\cdot}X$ is the only significant solar absorber with this vertical signature. The $O_2{\cdot}X$ heating rates in Figure 1 do not appear linear because they are expressed as functions of pressure rather than density.

Figure 1 shows that clouds significantly enhance $O_2{\cdot}X$ heating above cloud top and reduce heating beneath cloud

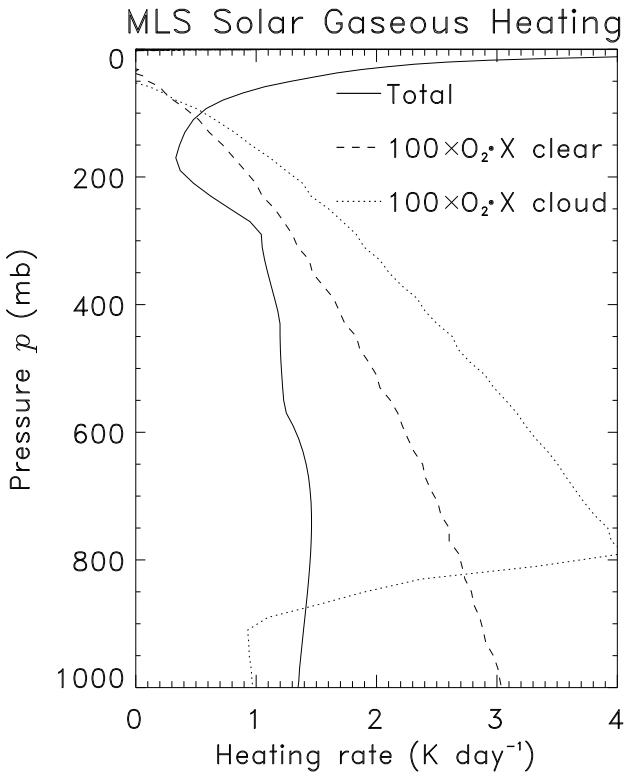


**Figure 1.** Vertical profile of solar gaseous heating (K $d^{-1}$) for a standard, climatological midlatitude summer atmosphere. Shown are the total solar heating rate in clear sky (solid) and, exaggerated by a factor of 100, the $O_2$·X contributions to the heating in clear sky (dashed) and in the presence of a 100 g $m^{-2}$, 100 mb thick stratus cloud (dotted).

top (dotted line). Thus clouds shift the $O_2$·X heating profile maximum upward to the level of the cloud top. This feature appears prominently in climatological averages of $O_2$·X heating shown in section 4.4.

In summary, $O_2$·X bands are present in much of the visible spectrum and in important near-infrared windows. These bands are well characterized by the linear limit of small absorber paths. The vertical profile of clear sky $O_2$·X heating weakly decreases the atmospheric stability.

### 3.3. Implementation of Absorption in GCM

To estimate the global abundance and forcing of $O_2$·X, we employed the National Center for Atmospheric Research (NCAR) Community Climate Model, Version 3 (CCM3) general circulation model [**?**]. The CCM3 employs an 18 bin $\delta$-Eddington approximation for the solar spectral region [**?**]. The eight bins for $\lambda < 0.7$ µm represent monochromatic intervals, but water vapor absorption in the near-infrared is represented by a seven bin $k$-distribution technique. We created binary cross sections $\overline{\sigma}$ for each CCM spectral bin by spectrally averaging $\sigma^b_{O_2\cdot X}(\lambda)$ from the laboratory resolution ($\sim 0.15$ nm) to the CCM resolution. The near-infrared 1.06 and 1.27 µm continuum absorption bands were mapped into the CCM $k$-distribution bins corresponding to the mean intensity of the nearest water vapor bands. This procedure included weighting the high-resolution cross sections by the incident solar flux at the top of the atmosphere in the more detailed narrow band multistream (NBM) model [**?**]. In offline single-column comparisons, the CCM3 radiation model and the NBM model $O_2$·X absorption agreed to within 10% for standard atmospheric conditions ranging from Arctic to Tropical, so no tuning of the $\overline{\sigma}$ was required.

## 4. Global Abundance and Absorption

The NCAR CCM3 general circulation model [**?**] has 18 levels in the vertical and a horizontal resolution of $\sim 2.8^\circ \times 2.8^\circ$ near the equator. The dynamical timestep is 20 min, but radiative fluxes are computed hourly. Cloud diagnosis is based on convective activity, stability, and relative and absolute humidity. Hydrometeor optical properties are partitioned into liquid and ice components based on temperature and pressure. **?** show that compared to observations, the CCM3 produces little or no bias in clear sky radiative fluxes and only small biases in cloudy sky fluxes. Thus the CCM3 is suitable for assessing the radiative forcing of other (noncloud) atmospheric constituents.

We performed three CCM integrations in order to separately estimate the forcings caused by $O_2$·$O_2$, $O_2$·$N_2$, and $O_2$·$O_2$ + $O_2$·$N_2$, respectively. Each integration is 1 year long and is initialized from the same fully spun up data set for January 1. The integrations employed climatological sea surface temperatures, and all forcings are seasonally averaged (i.e., 3 month means) in order to minimize the influence of variability on the results. The solar radiation physics were called twice each solar radiation time step (60 min): once with and once without $O_2$·X heating. $O_2$·X forcing is the difference between these values. We archived $O_2$·X abundance and forcing every times tep (20 min), but these forcings were not allowed to affect the predicted climate.

### 4.1. Annual Mean Abundance and Absorption

Collision complex abundance is a statistic of the second moment of dry air density (1). Plate 3 shows the annual mean column abundance of $O_2$·$O_2$, $N_{O_2\cdot O_2}$. The major meridional gradient is caused by the poleward decrease in zonal mean temperature. Cold polar air of a given mass is

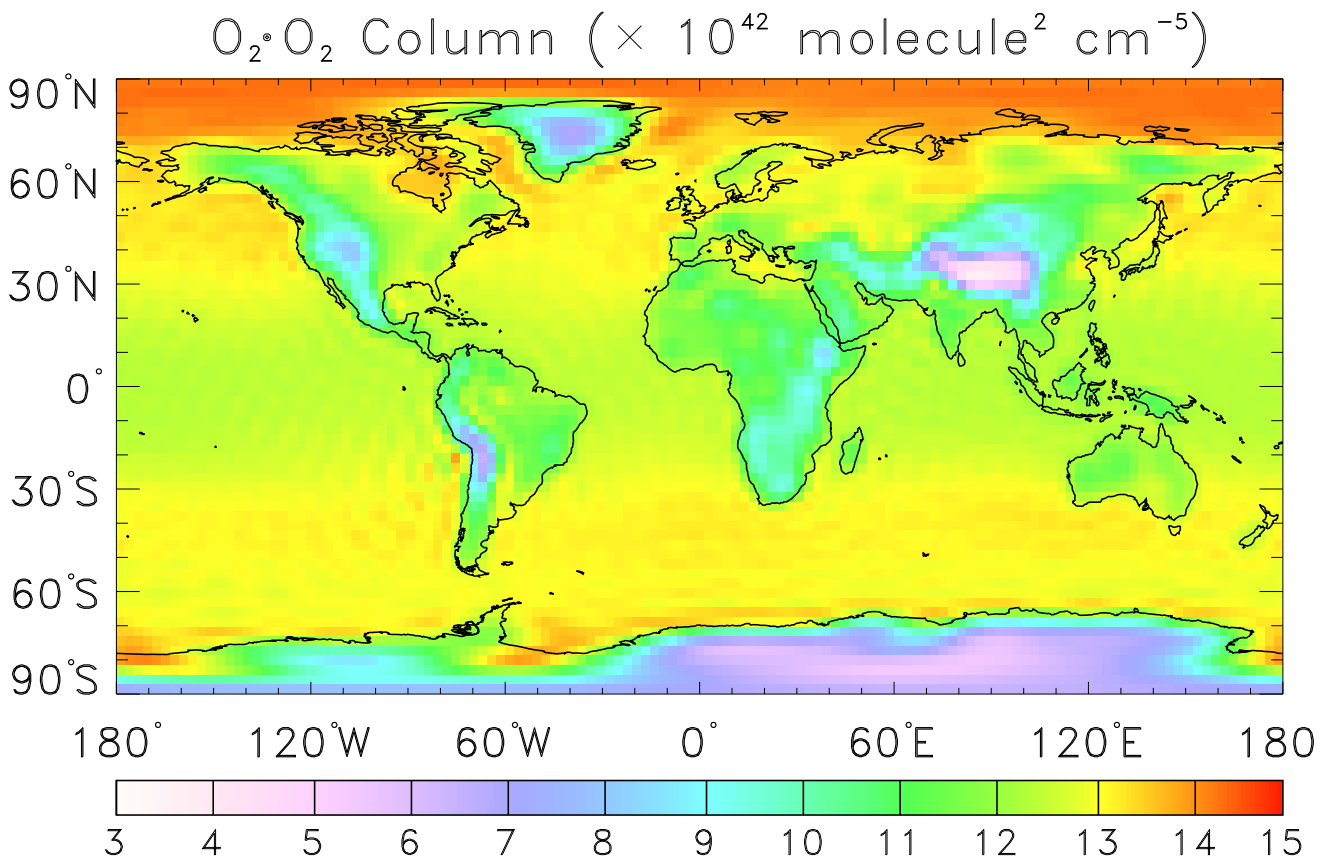


**Plate 3.** Annual mean column abundance $N_{\mathrm{O_2{\cdot}O_2}}$ ($\times 10^{42}$ molecule$^2$ cm$^{-5}$) of $\mathrm{O_2{\cdot}O_2}$.

denser than warm tropical air. Since $n_{\mathrm{O_2{\cdot}O_2}}$ is the square of $n_{\mathrm{O_2}}$ (1), $N_{\mathrm{O_2{\cdot}X}}$ is $\sim 20\%$ greater in the Arctic than the tropics at the same sea level pressure. The same would be true of the Antarctic, except the Antarctic plateau displaces the densest portion of the troposphere, significantly reducing $\mathrm{O_2{\cdot}X}$ column abundance. The Tibetan Plateau, Greenland, East Africa, the Andes, and the Rockies also show significant orographic reduction in $N_{\mathrm{O_2{\cdot}X}}$. Note that orographic reduction of $N_{\mathrm{O_2{\cdot}X}}$ is time-invariant, in contrast to effects of seasonally varying temperature and pressure in the extratropics, discussed below. Whereas the zonal mean column abundance of a well-mixed molecule (e.g., $N_{\mathrm{O_2}}$) decreases by $30\%$ from sea level in the Arctic to the Antarctic plateau at 700 mb, the corresponding decrease in $N_{\mathrm{O_2{\cdot}X}}$ exceeds 50%. In summary, $\mathrm{O_2{\cdot}X}$ is more sensitive to the thermodynamic and orographic environment than $\mathrm{O_2}$ or $\mathrm{N_2}$ alone, owing to its quadratic dependence on these constituents.

Uncertainties in simulated $N_{\mathrm{O_2{\cdot}X}}$ stem from biases in model pressure $p$, temperature $T$, and surface elevation. The maximum seasonal mean CCM temperature bias in the lower troposphere is $< 6\,\mathrm{K}$ [**?**]. The maximum seasonal mean CCM grid point surface pressure bias is $< 1\%$ [**?**]. Biases in column $\mathrm{O_2}$ arising from the discretization of surface elevation do not exceed 1%. Assuming the worst case scenario (errors are additive) yields a conservative uncertainty in seasonal grid point mean $N_{\mathrm{O_2}}$ and $N_{\mathrm{N_2}}$ of $\pm 4\%$, implying uncertainty bounds for $N_{\mathrm{O_2{\cdot}O_2}}$ and $N_{\mathrm{O_2{\cdot}N_2}}$ of $\pm 8\%$. The maximum uncertainty is over the Antarctic shelf and the Tibetan Plateau, regions where variability and differences with climatological analyses are relatively large [**?**]. The simulated annual mean surface pressure is 984.5 mb, in excellent agreement with 984.9 mb from National Centers for Environmental Prediction (NCEP) reanalyses. This confirms that grid point biases in $N_{\mathrm{O_2{\cdot}X}}$ are generally random, not systematic, and we place the global mean bias conservatively at $\pm 2\%$. As will be described below, grid point biases in simulated $\mathrm{O_2{\cdot}X}$ forcing are generally dominated by uncertainties in absorber cross section and cloud vertical distribution, not $\mathrm{O_2{\cdot}X}$ abundance.

The regional abundance of any well-mixed collision com-

**Table 1.** Global Annual Mean Abundances of Well-Mixed Collision Complexes

| Complex X·Y | Scale $N_{X\cdot Y}/N_{O_2\cdot O_2}$ | Abundance, molecule$^2$ cm$^{-5}$ | Collision Induced Absorption Bands |
|---|---|---|---|
| $O_2$·$O_2$ | 1 | $1.24 \times 10^{43}$ | HC, 1.58 µm 6.42 µm |
| $O_2$·$N_2$ | 3.728 | $4.62 \times 10^{43}$ | HC, 4.29 µm, 6.42 µm, 100 cm$^{-1}$ |
| $N_2$·$N_2$ | 13.90 | $1.72 \times 10^{44}$ | 4.29 µm, 90 cm$^{-1}$ |
| $O_2$·Ar | 0.0446 | $5.52 \times 10^{41}$ | HC, 1.27 µm, 6.42 µm |
| $O_2$·$CO_2$ | $1.69 \times 10^{-3}$ | $2.09 \times 10^{40}$ | 1.27 µm |
| $O_2$·$CH_4$ | $8.1 \times 10^{-6}$ | $1.00 \times 10^{38}$ | HC |
| $CO_2$·$CO_2$ | $2.87 \times 10^{-6}$ | $3.55 \times 10^{37}$ | 60 cm$^{-1}$ |

Scale factors relate $N_{X\cdot Y}$ to $N_{O_2\cdot O_2}$ (1). Band locations are approximate centers of absorption bands. HC denotes Herzberg Continuum ($\sim$ 200–250 nm). $O_2$·$O_2$ and $O_2$·$N_2$ bands considered in this study (Plate 1) are omitted for brevity. Spectral data compiled from **?**, **?**, **?**, **?**, **?**, **?**, and **?**.

plex X·Y is determined by scaling Plate 3 by the product of the ratios $n_X/n_{O_2}$ and $n_Y/n_{O_2}$. Table 1 summarizes the scale factors (relative to $O_2$·$O_2$) and global annual mean abundances of many well-mixed collision complexes. The scale factors were computed using atmospheric abundances of **?** [**?**, p. 9], corrected to present-day values in the case of $CO_2$ (355 ppm) and $CH_4$ (1.7 ppm).

The final column of Table 1 lists the approximate centers of the collision induced absorption bands due to each complex, apart from the $O_2$·X bands shown in Plate 1. Taken together, such bands appear in the spectrum from the Herzberg continuum to the far infrared. In addition to the bands shown in Plate 1, collisions involving $O_2$·$O_2$ and $O_2$·$N_2$ induce oxygen absorption in the Herzberg continuum from 195 to 250 nm and in the oxygen (forbidden) fundamental vibration band at 6.42 µm [**??**]. Both $O_2$·$N_2$ and $N_2$·$N_2$ induce absorption in the nitrogen (forbidden) fundamental band at 4.29 µm. Insolation in these spectral regions is too weak to allow significant solar absorption in absolute terms. However, it may be important to account for this absorption when retrieving atmospheric parameters such as temperature from remotely sensed spectra, for example, in the $CO_2$ 4.3 µm band [**?**, p. 192].

Plate 4 shows the annual mean increase in atmospheric absorption due to $O_2$·X. The annual mean forcing approximately resembles the abundance (Plate 3), though some new features are evident. First note the enhanced atmospheric absorption above bright, low surfaces (desert, stratus clouds, ice). Since the spectral optical depth of most $O_2$·X bands is $< 0.05$ (Plate 2), absorption in these bands is in the linear limit where a change in absorber path causes a proportionate change in atmospheric absorption. Reflection from low, bright surfaces increases photon path lengths in the $O_2$·X-rich lower atmosphere. This increases the mean $O_2$·X path and thus the $O_2$·X absorption. However, reflection from high clouds (e.g., tropical cirrus) prevents photons from reaching the lower atmosphere and reduces the mean $O_2$·X path traversed by these photons. This reduces $O_2$·X absorption and causes the local minima in $O_2$·X forcing in the Intertropical Convergence Zone (ITCZ) region. The zonal annual mean atmospheric absorption due to $O_2$·X is $\sim$ 0.9 W m$^{-2}$ and does not vary strongly with latitude (not shown).

It is interesting to note that geographic structure of $O_2$·$N_2$ absorption closely resembles that of $O_2$·$O_2$ absorption, so that their sum, Plate 4, adequately represents the structure of each. Since $O_2$·$N_2$ absorption occurs entirely in the 1.27 µm band, it is enhanced relative to $O_2$·$O_2$ over vegetated surfaces but diminished over sea-ice and ocean due differences between the near-infrared and visible albedos of these surfaces. The magnitude of global mean $O_2$·$N_2$ absorption is proportional to the assumed $N_2$ efficiency. This study assumes $\epsilon_{N_2} = 0.2$, which leads to $O_2$·$N_2$ forcing being 20% of $O_2$·$O_2$ absorption. As discussed in section 2.2, $\epsilon_{N_2}$ may be 0.3, in which case $O_2$·$N_2$ forcing would be 30% of $O_2$·$O_2$ forcing.

It is useful to distinguish atmospheric absorption from other common metrics of radiative forcing. Table 2 summarizes the global mean statistics of $O_2$·X atmospheric forcing, surface forcing, column radiative forcing, and net radiative forcing at the tropopause. The first row, atmospheric forcing, is the mean increase in atmospheric absorption due to $O_2$·X (Plate 4), 0.93 W m$^{-2}$. For comparison, the all sky solar absorption due to $H_2O$, $O_3$, $O_2$, and $CO_2$ is $\sim$ 43, 14, 2, and 0.5 W m$^{-2}$, respectively [**?**] ($NO_2$ abundance is highly heterogeneous and a reliable estimate of its mean ab-

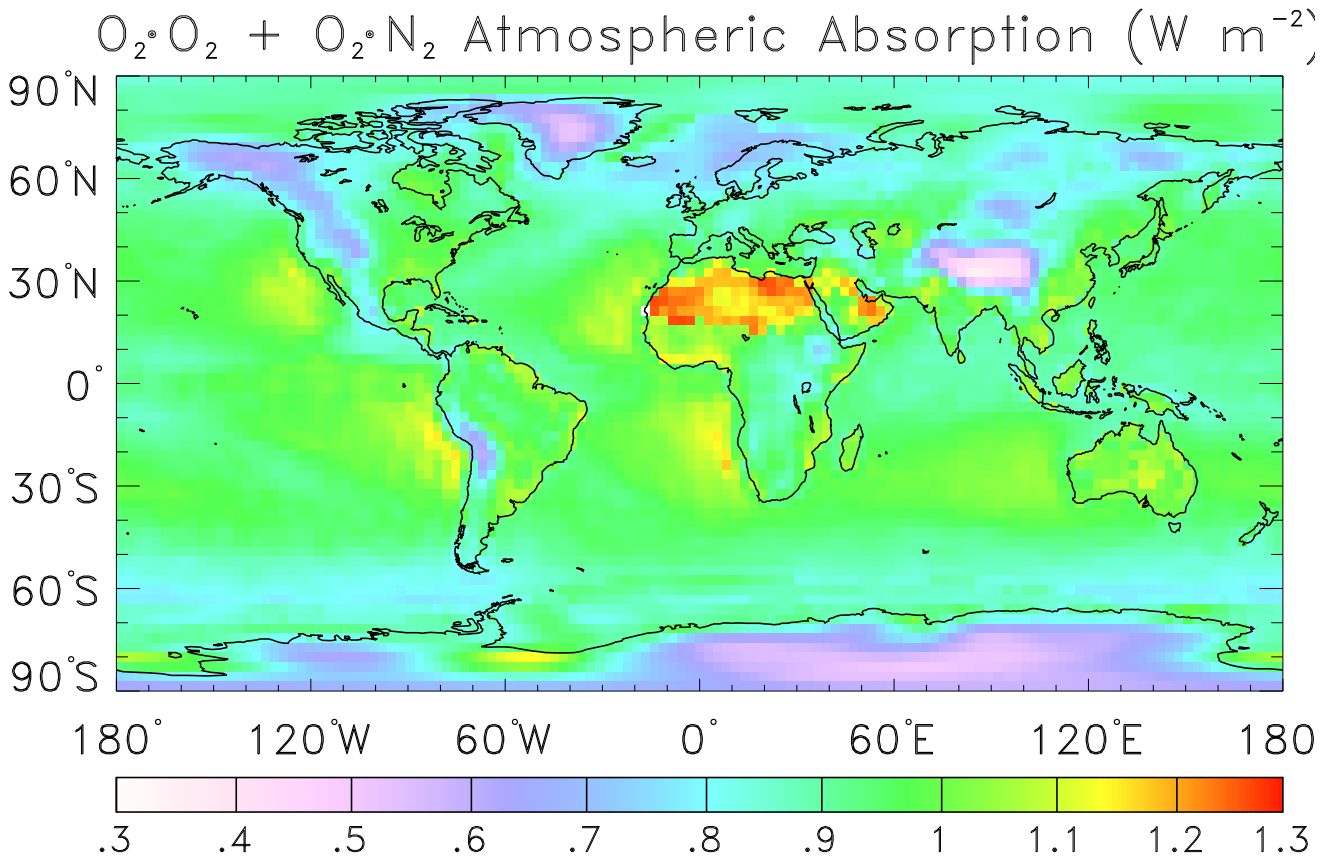


**Plate 4.** Annual mean increase in column atmospheric absorption (W m$^{-2}$) due to $O_2{\cdot}X$.

sorption has yet to be made). The second row shows that on average, the clear sky atmospheric absorption by $O_2{\cdot}X$ slightly exceeds the all sky absorption.

Atmospheric absorption at solar wavelengths reduces surface insolation (third row of Table 2) and thus surface absorption (fourth row). The fifth row shows the column radiative forcing, the sum of atmospheric forcing and surface forcing. This quantity (column radiative forcing) equals the change in net radiative flux at the top of the atmosphere. The impact of atmospheric constituents on tropospheric climate is, by convention, quantified by the change in net radiative flux at the tropopause, shown in row six. More than 97% of $O_2{\cdot}X$, and thus 97% of $O_2{\cdot}X$ absorption, is in the troposphere (see Plate 6). Therefore the column radiative forcing of $O_2{\cdot}X$ nearly equals the net radiative forcing at the tropopause.

### 4.2. Uncertainty in Mean $O_2{\cdot}X$ Forcing

The largest uncertainties in the estimates in Table 2 stem from uncertainties in cross section $\sigma^b_{O_2{\cdot}O_2}$, $N_2$ efficiency $\epsilon_{N_2}$, $O_2{\cdot}X$ abundance $N_{O_2{\cdot}X}$, and cloud vertical distribution. The uncertainty ranges for these quantities are $\sigma^b_{O_2{\cdot}O_2}(\lambda)$, $-30$ to $+10\%$, depending on $\lambda$ (see section 2.2); $\epsilon_{N_2}$, $\pm 50\%$; and $N_{O_2{\cdot}X}$, $\pm 2\%$. Also, appending the $O_2{\cdot}O_2$ 1.58 µm continuum of **?** to the **?** cross sections would increase our computed total $O_2{\cdot}X$ solar forcing by $\sim 4\%$. As discussed in section 2.1, the possible temperature dependence of $\sigma^b_{O_2{\cdot}X}(\lambda)$ is not yet fully understood [**???**]. Therefore we have not included uncertainty due to possible temperature dependence of $\sigma^b_{O_2{\cdot}X}$ in our error analysis.

The simulated mean clear sky and all sky planetary albedos agree with satellite observations to within 0.005 [**?**], eliminating the possibility of gross surface or cloud reflectance biases in estimated $O_2{\cdot}X$ forcing. Modeled total cloud fraction, 0.588, is bracketed by the Nimbus 7 and International Satellite Cloud Climatology Project (ISCCP)

**Table 2.** Global Annual Mean Forcings of $O_2$·X

| Forcing, W m$^{-2}$ | $O_2$·$O_2$ | $O_2$·$N_2$ | Total |
|---|---|---|---|
| Atmospheric Absorption | 0.78 | 0.15 | 0.93 |
| (same, but for clear sky) | (0.78) | (0.17) | (0.94) |
| Surface Insolation | −0.50 | −0.10 | −0.60 |
| Surface Absorption | −0.42 | −0.08 | −0.51 |
| Sfc. + Atm. Absorption | 0.36 | 0.07 | 0.42 |
| Net Flux at Tropopause | 0.34 | 0.06 | 0.40 |

Total forcings may be up to 20% lower or 30% higher than indicated. See text for uncertainty analysis. Sfc, surface; Atm, atmosphere.

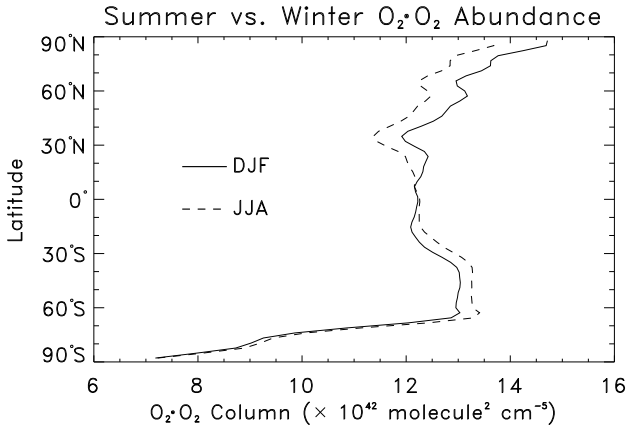


**Figure 2.** Zonal mean column abundance of $O_2$·$O_2$, $N_{O_2\cdot O_2}$ ($\times 10^{42}$ molecule$^2$ cm$^{-5}$), for DJF (solid line) and JJA (dashed line).

estimates of 0.522 and 0.625, respectively [**?**]. The vertical distribution of cloudiness generally agrees with observations for clouds below 400 mb but disagrees for cloud top heights above 400 mb, a region where clouds efficiently reduce $O_2$·X forcing. The CCM high cloud fraction, 0.34, exceeds ISCCP analyses by 0.20 [**?**]. There is considerable uncertainty in the observations, but if the ISCCP total and high cloud estimates are correct, then we estimate the modeled all sky $O_2$·X forcing is up to 10% too low because of exaggerated amounts of high-level cloud relative to low-level cloud.

Except for $O_2$·X abundance, the aforementioned uncertainties are systematic, not random. Summing the uncertainties for a conservative error estimate yields a total uncertainty range for the all sky forcings in Table 2 of $-20$ to $+30\%$. Thus the uncertainty range for $O_2$·X all sky absorption is 0.75–1.21 W m$^{-2}$. The lower bound forcing corresponds to the 1.06 and 1.27 µm $\sigma^b_{O_2\cdot X}$ of **?** and $N_2$ efficiency $\epsilon_{N_2} = 20\%$ (3). The upper bound forcing uses $\sigma^b_{O_2\cdot X}$ from **?** and **?**, $\epsilon_{N_2} = 30\%$, and assumes that 4% of $O_2$·X absorption occurs at 1.58 µm and that the CCM3 overpredicts high level clouds relative to low-level clouds.

The results in Table 2 appear to contrast with two prior studies. **?** estimate $O_2$·$O_2$ enhances all sky heating relative to clear sky heating by $\sim 7\%$ (neglecting the 1.27 µm band). Using identical $O_2$·X cross sections to our study, **?** estimated the mean atmospheric absorption due to $O_2$·X is 0.9–1.3 W m$^{-2}$. Both these prior studies used the same method to convert single-column results to global mean results. The method assumes 50% of the globe is covered with cloud top heights at 700 mb and that these clouds increase the photon path by 30 km [**?**]. Thus their conversion method assumes fewer and lower clouds than predicted by the CCM3. These assumptions both lead to larger forcings than shown in Table 2 and, taken together, suffice to explain the differences between the studies. It is unclear whether assumptions regarding surface albedo and elevation also contribute to these model differences.

### 4.3. Seasonal Structure of Abundance and Absorption

Owing to the seasonal cycles of insolation and temperature, annual mean forcings do not suffice to characterize the geographic and vertical distribution of $O_2$·X forcing as it impacts the climate system. To illustrate this point, Figure 2 shows the zonal mean of the column abundance of $O_2$·$O_2$ for December–February (DJF) and June–August (JJA). The increases in $N_{O_2\cdot X}$ from summer to winter in the North and South polar regions are 8–10% and 1–3%, respectively. These increases are entirely due to seasonal changes of pressure and temperature. Although the solar radiative forcing of $O_2$·X during polar winter is zero, this seasonal cycle in $N_{O_2\cdot X}$ does affect $O_2$·X absorption bands in the far infrared (see Table 1) throughout the year. The meridional gradient and seasonal changes in $N_{O_2\cdot X}$ depicted in Figure 2 apply to all other collision complexes in Table 1 as well.

The strongest modulator of solar radiative forcing is, of course, the seasonal change of insolation. Plate 5 shows the geographic distribution of the seasonal mean atmospheric absorption by $O_2$·X. $O_2$·X absorption is greatest in polar regions in summer, where peak insolation coincides with the greatest $O_2$·X abundances (Figure 2). Plates 5a and 5c show southern and northern summer forcings are nearly symmetric about the equator. Arctic forcing is 10–30% stronger than Antarctic forcing, mainly the Antarctic plateau reduces $N_{O_2\cdot X}$. Most remarkable are the large polar regions where atmospheric $O_2$·X absorption approaches or exceeds 2.0 W m$^{-2}$ on seasonal timescales. Seasonal sea

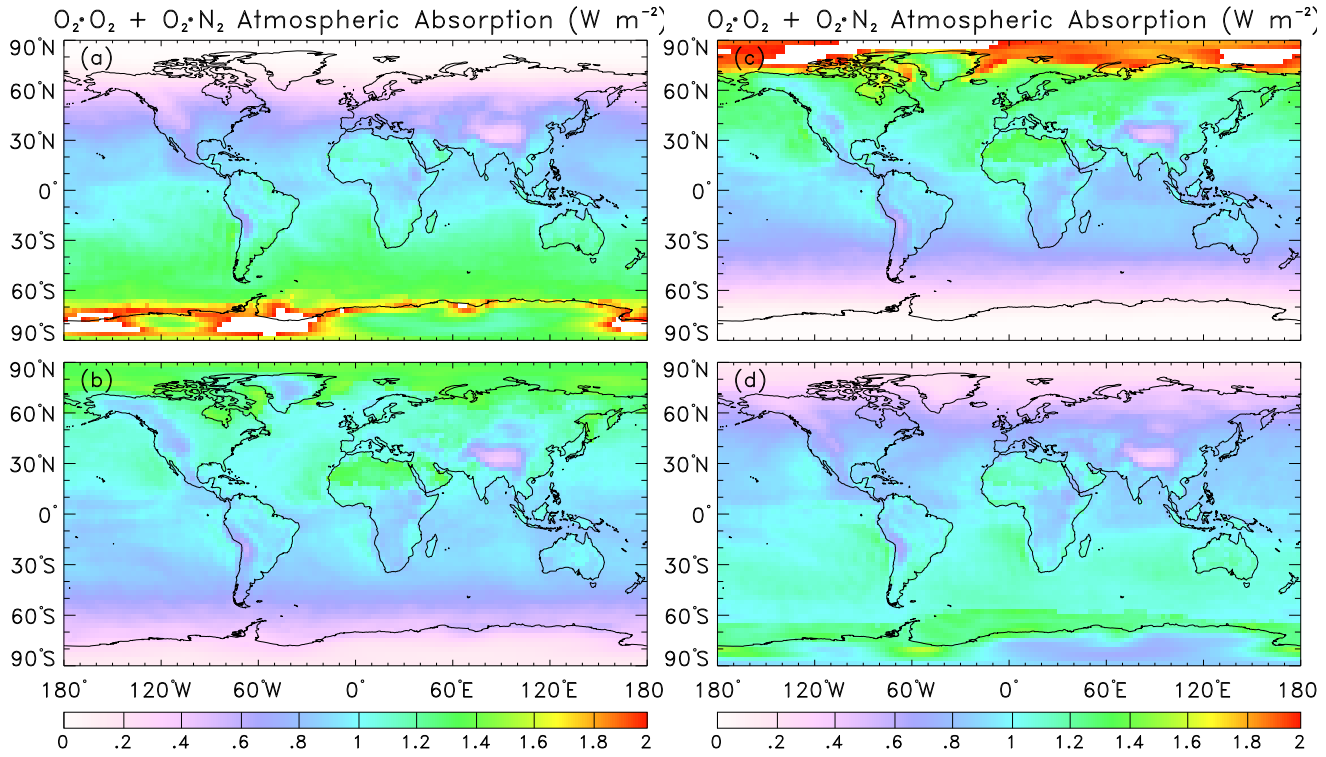


**Plate 5.** Seasonal mean increase in atmospheric solar absorption (W $m^{-2}$) due to $O_2{\cdot}X$. (a) December–February (DJF). (b) March–May (MAM). (c) June–August (JJA). (d) September–November (SON). White regions exceed maximum scale value by $< 0.7\,W\,m^{-2}$.

ice boundaries appear in Plates 5a–5d where they demarcate the open ocean from regions of higher absorption. Equinoctial forcings (Plates 5b and 5d) extend farther into the winter hemisphere than solstitial forcings, and are weaker.

Surface albedo, elevation, and clouds all play roles in determining the seasonal forcing maxima near the poles. To help disentangle these roles, we show in Figure 3 the zonal mean of the winter and summer seasonal forcings (Plates 5a and 5c) due to $O_2{\cdot}X$. The influence of clouds and surface albedo on $O_2{\cdot}X$ forcing is clarified by comparing the seasonal forcings in Figure 3 to the seasonal abundances in Figure 2. The zonal mean summertime $O_2{\cdot}X$ forcing in the Antarctic (70–90°S), 1.69 W $m^{-2}$, is 96% of the forcing in the Arctic (70–90°N), 1.76 W $m^{-2}$, although the Antarctic has only 74% of the $O_2{\cdot}X$. Thus surface and low-level cloud reflectance makes $O_2{\cdot}X$ forcing 30% more efficient (per unit abundance) in the Antarctic than in the Arctic. Within 5° of the poles, the forcing efficiency of $O_2{\cdot}X$ is 75% greater in the Antarctic than in the Arctic. The change in forcing efficiency reduces, and nearly eliminates, the surface elevation-induced disparity in forcing between the poles.

The large difference between the forcing efficiencies of $O_2{\cdot}X$ in the Arctic and the Antarctic is caused by differences in the surface albedo, cloud distribution, and water vapor column between the two polar climate systems. First, the simulated visible surface albedo of Arctic sea ice is $\sim 0.6$, much lower than the simulated visible surface albedo of the Antarctic continent, $\sim 0.95$ [**?**]. Offline sensitivity studies show that in the absence of clouds, the higher surface reflectance underlying Antarctic $O_2{\cdot}X$ increases forcing (per unit abundance) by $\sim 25\%$ relative to the Arctic. Observations suggest the modeled surface albedo and low-level cloud fraction in the summertime Arctic are $\sim 0.15$ and 0.10 too high, respectively [**?**]. This suggests the simulated summertime Arctic forcing is too high, which would amplify the disparity between Arctic and Antarctic forcing efficiencies.

A second, but much weaker, effect is due to the change in simulated precipitable water content from the summertime Arctic (11.5 kg $m^{-2}$) to the Antarctic (2.7 kg $m^{-2}$). Both are in fair agreement with European Centre for Medium-Range Weather Forecasts (ECMWF) analyses [**?**]. The drier Antarctic column makes the wings of the near-infrared water

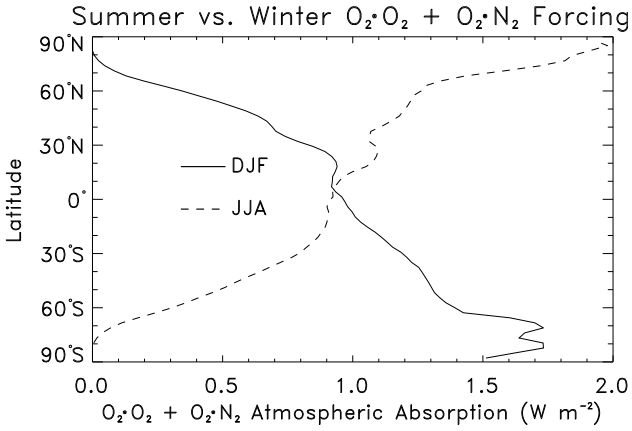


**Figure 3.** Zonal seasonal mean increase in atmospheric solar absorption (W $m^{-2}$) due to $O_2$·X: DJF (solid line) and JJA (dashed line).

vapor bands (compare Plate 2) more transmissive (less saturated). This increases absorption per unit $O_2$·X by $\sim 2\%$.

### 4.4. Vertical Structure

The vertical profile of $O_2$·X heating is important in determining possible dynamical feedbacks as well as the change in net flux at the tropopause. Plate 6 shows the vertical profile of the seasonally and zonally averaged solar heating due to $O_2$·X. The vertical axis is the CCM hybrid vertical coordinate times 1000 [**?**]. Thus the panels transition from a pure sigma coordinate representation at the surface to a pure pressure representation near 200 mb. As mentioned previously, virtually all of the heating is confined to the troposphere. $O_2$·X heating decreases toward the winter hemisphere due to decreasing daylight hours. Above 700 mb (300 mb above the surface) the heating decreases with pressure due to decreasing $O_2$·X abundance (compare Figure 1). Seasonal $O_2$·X heating in excess of 0.02 K $d^{-1}$ extends throughout the polar summer troposphere. This is 2–4% of local solar heating owing to all other solar absorbers (compare Figure 1). The heating rate in the Antarctic summer troposphere (Plate 6a) is nearly 20% stronger than the Arctic summer troposphere (Plate 6c) due to its thinner atmosphere.

The heating peaks between 200–300 mb above the surface in all regions every season. This peak does not coincide with the maximum $O_2$·X abundance (which is always at the surface) even though $O_2$·X absorption is in the optically thin limit (Plate 2). As shown in Figure 1, the location of maximum $O_2$·X heating does coincide with maximum $O_2$·X abundance except when efficient scatterers such as clouds screen the $O_2$·X in the lower atmosphere from incoming solar radiation. Thus cloud reflection is responsible for shifting the mean vertical location of maximum $O_2$·X absorption, and thus heating, upward from the surface by 200–300 mb. Plate 6 supports this by showing that the heating maxima as a function of latitude dips somewhat closer to the surface in the subtropical regions characterized by large-scale subsidence and relatively clear skies.

Radiative forcing in other nonoverlapped, optically thin bands of well-mixed collision complexes (e.g., the $N_2$·$N_2$ fundamental band at 4.29 μm, see Table 1), will show qualitatively similar patterns to Plates 4–6. The magnitude of forcing by other bands is, of course, highly sensitive to the spectral location of the particular band.

## 5. Discussion and Summary

We have characterized the spectral, vertical, regional, and seasonal atmospheric heating by $O_2$·X. The motivations for modeling the global distribution and forcing of $O_2$·X were to refine and extend estimates of $O_2$·X forcing inferred from one-dimensional studies to the global climate scale. Our global simulations indicate that global annual mean atmospheric absorption by $O_2$·X is 0.75–1.2 W $m^{-2}$ (Table 2). This falls between the recent estimates of 0.9–1.3 W $m^{-2}$ [**?**] and 0.84 W $m^{-2}$ [**?**]. This absorption reduces surface insolation by 0.48–0.78 W $m^{-2}$.

$O_2$·X absorption is highly localized in the troposphere and it increases the net radiative flux at the tropopause by 0.32–0.52 W $m^{-2}$. It is useful to compare this absolute radiative forcing by $O_2$·X (whose abundance is not changing) to greenhouse gas forcing (due to changes in the gases' abundance from preindustrial to present-day levels). This comparison enables us to assess the magnitude of the perturbation to the mean state climate caused by $O_2$·X. The 0.32–0.52 W $m^{-2}$ forcing by $O_2$·X is less than the anthropogenic forcing of $CO_2$ (1.75 W $m^{-2}$) but comparable to forcing by $CH_4$ (0.44 W $m^{-2}$), stratospheric $H_2O$ (0.15 W $m^{-2}$), and $N_2O$ (0.11 W $m^{-2}$) [**?**, p. 57].

By extending the simulations to the global scale, we were able to characterize the spatial and temporal distributions of $O_2$·X abundance and forcing. $O_2$·X abundance mimics the concentration of $O_2$ and $N_2$, except its quadratic dependence on these constituents accentuates both its spatial and temporal gradients. This dependence causes a 20% increase in $O_2$·X abundance in the Arctic relative to the Tropics for the same sea level pressure. $O_2$·X abundance depends most on zonal mean temperature, pressure, and surface elevation. The variations in zonal mean $O_2$·X abundance due to surface elevation, the annual mean meridional temperature gradient, and to seasonal temperature variations are 40, 15, and 10%, respectively. These results scale to all collision complexes

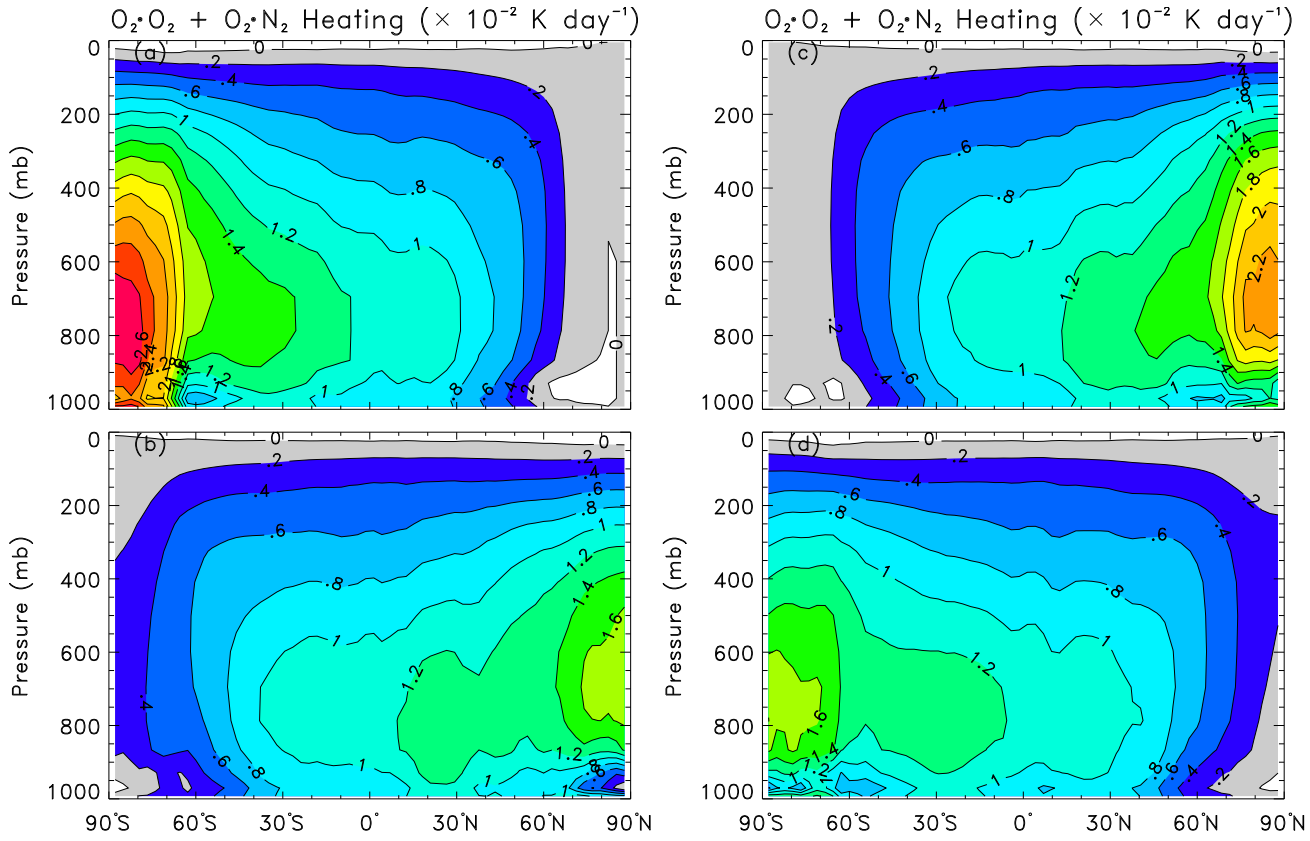


**Plate 6.** As in Plate 5, but for the vertical profile of the heating ($\times 10^{-2}$ K d$^{-1}$) due to $O_2 \cdot X$.

of well-mixed gases, for example, $N_2 \cdot N_2$ and $O_2 \cdot Ar$.

Many features of $O_2 \cdot X$ radiative forcing are common to all solar absorbers, but the relatively sharp gradients in $O_2 \cdot X$ abundance enhance these features. Surface and cloud reflectance modulate the solar forcing efficiency of $O_2 \cdot X$ (forcing per unit abundance) by altering the mean $O_2 \cdot X$ path traversed by the average photon. These factors explain why annual mean collision complex forcing peaks in the subtropics over bright deserts and regions of marine stratus. The seasonal cycle of insolation causes the seasonal mean solar forcing to peak in summertime polar regions. However, these summertime polar peaks are enhanced by bright surfaces and extensive low-level clouds, especially in the Arctic. The forcing efficiency of complexes in the Antarctic is 30–75% greater than in the Arctic.

In clear skies the magnitude of $O_2 \cdot X$ heating grows linearly with air density, peaking at the surface. This heating profile tends to weakly destabilize the atmospheric column. On seasonal timescales, clouds shift the height of peak $O_2 \cdot X$ heating upward by 200–300 mb and smooth out the vertical decrease of heating that would otherwise follow the rapid decrease of $O_2 \cdot X$ abundance with height. $O_2 \cdot X$ heating peaks at 0.02–0.03 K d$^{-1}$ in the polar troposphere in summer. This is 2–4% of local heating due to all other solar absorbers.

Many GCMs have strong cold biases at the summertime polar tropopause, where the CCM3 (not shown) is up to 10–14 K too cold [**?**]. The CCM3 also suffers from a cold bias in the summertime polar troposphere of 2–6 K [**?**]. Some, but probably not all, of these biases are due to the numerical treatment of dynamics [**?**]. It is likely that allowing $O_2 \cdot X$ heating to affect the thermal structure of the atmosphere will ameliorate, though not eliminate, the remainder of these biases. For example, single-column simulations show the radiative relaxation timescale at the polar tropopause is $\sim 50$ days. Thus the $O_2 \cdot X$ heating of $\sim 0.01$ K d$^{-1}$ (Plate 6) increases the radiative equilibrium temperature by $\sim 1$ K in this region.

We quantified some fingerprints that distinguish absorption due to well-mixed collision complexes (and well-mixed dimers) from absorption due to well-mixed monomers. The most significant distinguishing feature is the stronger spatial and temporal gradients of collision complex abundance

relative to monomer abundance. Whereas the zonal mean column abundance of a well-mixed molecule such as $O_2$ decreases by 30% from sea level in the Arctic to the Antarctic plateau at 700 mb, the corresponding decrease in $N_{O_2\cdot X}$ exceeds 50%. In the weakly absorbing, nonoverlapped limit, well-mixed molecules cause an increase in the solar heating rate that is constant with air density, whereas well-mixed collision complexes such as $O_2$·X cause the solar heating rate to increase linearly with air density.

**?** demonstrated that $O_2$·$O_2$ absorption improved agreement between modeled and observed solar absorption in both clear and cloudy skies during the Atmospheric Radiation Measurement (ARM) Enhanced Shortwave Experiment (ARESE). Their total (direct + diffuse) clear sky surface insolation discrepancies ($\sim 15\,\mathrm{W\ m^{-2}}$) were no larger than instrumental and model uncertainties (e.g., aerosol properties). Working with an independent set of radiometric observations from ARESE, **?** found excellent model agreement with direct beam observations but reported a $30\,\mathrm{W\ m^{-2}}$ model overestimate of the instantaneous diffuse surface insolation during clear sky conditions over multiple days during ARESE. They did not account for $O_2$·X absorption. As shown in section 3.1, $O_2$·X absorption reduced clear sky noontime surface insolation by $\sim 2\,\mathrm{W\ m^{-2}}$ during ARESE. However, nearly 90% of this $O_2$·X absorption came from the direct solar beam, and only 10% occurred in the diffuse field. This illustrates the point that unknown or neglected gaseous absorption processes cannot, by themselves (i.e., without invoking aerosol processes), remedy a clear sky diffuse radiation bias because gaseous absorption of the direct beam far exceeds gaseous absorption of the diffuse field.

Our global simulations show that in the annual mean, $O_2$·X enhances absorption equally in clear and cloudy skies. Thus $O_2$·X neither exacerbates nor remediates solar absorption discrepancies that are associated with clouds [**???**]. The agreement between clear and cloudy sky $O_2$·X absorption is due to the global mean cancellation of photon and absorber path length changes due to clouds: Low-level clouds increase $O_2$·X absorption relative to clear skies by increasing path lengths, while middle- and high-level clouds decrease $O_2$·X absorption by screening photons from the lower atmosphere. We hypothesize that this agreement is predominantly due to the global vertical distributions of cloud reflectivity and well-mixed molecules and has little to due with spectral features particular to $O_2$·X. There are two reasons to expect that this hypothesis is true. First, $O_2$·X absorption occurs at many locations in the visible and near-infrared and is not correlated with water vapor or condensate absorption bands. Second, cloud transmission is nearly spectrally uniform for $0.3 < \lambda < 1.5\,\mu\mathrm{m}$, so clouds do not preferentially transmit any energetically significant solar wavelength bands to the lower atmosphere. This hypothesis should be tested because, if it is true, it implies that globally averaged, well-mixed collision complexes or dimers do not enhance absorption more in cloudy sky than in clear sky. A similar hypothesis may hold for well-mixed molecules in general.

The radiative importance of other abundant, but not necessarily well-mixed, collision complexes and dimers in the atmosphere should be explored. **?** point out that Ar and $CO_2$ are also relatively efficient partners for inducing $O_2$ absorption at 1.27 μm but note that $O_2$·Ar and $O_2$·$CO_2$ are too scarce (Table 1) to cause significant absorption. **?** and **?** suggest $O_2$·$H_2O$ and $(H_2O)_2$ as promising candidates to examine in the search for neglected solar absorbers.

In summary, the recent discovery that the oxygen collision pairs $O_2$·$O_2$ and $O_2$·$N_2$ absorb a small but significant fraction of the globally incident solar radiation alters the long-standing view that $H_2O$, $O_3$, $O_2$, $CO_2$, and $NO_2$ are the only significant gaseous solar absorbers in Earth's atmosphere. This study quantified the spectral, regional, vertical, and seasonal patterns of $O_2$·X abundance and radiative forcing. We now know that globally and annually averaged, $O_2$·X absorbs about $1\,\mathrm{W\ m^{-2}}$ of solar radiation, more than $CO_2$, and that $O_2$·X does not increase cloudy sky solar absorption relative to clear sky absorption. Improved measurements of $O_2$·X absorption cross sections in the near infrared will remove about half of the 25% uncertainty in total $O_2$·X absorption. Accounting for $O_2$·X reduces discrepancies between models and measurements of solar absorption. $O_2$·X absorption should therefore be included in high-resolution radiative transfer models, remote-sensing retrieval algorithms, and in large-scale atmospheric models used to simulate climate and climate change. $O_2$·X has the most potential to improve the simulated climate in summertime polar regions. Future versions of the CCM will include this absorption.

**Acknowledgments.** S. Solomon and R. Portmann provided $O_2$·X cross section data and helpful suggestions at an early stage of this study. J. Burkholder, E. Mlawer, D. Newnham, and K. Pfeilsticker provided useful comments on $O_2$·$O_2$ cross section measurements and uncertainties. B. Briegleb, W. Collins, and S. Solomon made numerous suggestions which improved the quality of the manuscript. R. Portmann and one anonymous reviewer provided constructive reviews. The NCAR ASP program provided support and encouragement. This research was supported in part by DOE ARM Program Grant DEFG0593ER61376.